Supporting Information

for

"Organized Trade Cumulus Clouds Suppressed by Climate Change"

Jan Kazil[1,2], Pornampai Narenpitak[3], Takanobu Yamaguchi[1,2], and Graham Feingold[2]

[1] Cooperative Institute for Research in Environmental Sciences, University of Colorado Boulder, Boulder, Colorado, 80309, USA

[2] National Oceanic and Atmospheric Administration, Chemical Sciences Laboratory, Boulder, Colorado, 80305, USA

[3] Data-driven Simulation and Systems Research Team, National Electronics and Computer Technology Center, Pathumthani, 12120, Thailand

Contents of this file

1 Model, trajectories, forcings, and simulations

We use the System for Atmospheric Modeling [SAM, Khairoutdinov and Randall, 2003], version 6.10.10, to run Lagrangian large eddy simulations. Cloud microphysics is described using a two-moment method which represents the cloud and rain mode with lognormal functions [Feingold et al., 1998]. The cloud microphysics interacts with aerosol by activation, cloud processing, release upon droplet evaporation, and wet deposition. Radiation is calculated from temperature, gas phase constituents, and liquid water mass and effective radius with the Rapid Radiative Transfer Model [Iacono et al., 2008, Mlawer et al., 1997]. Greenhouse gas (GHG) species in the radiation calculation are CO_2, CH_4, N_2O, and O_3. The model calculates interactive surface fluxes of heat, moisture, momentum, and of sea spray aerosol. The model is described in further detail in Kazil et al. [2021].

The Lagrangian simulations were conducted along two trajectories (Fig. SF1). The simulations $\mathcal{F}_{\mathrm{PD}}$, $\mathcal{F}^{-}_{\mathrm{EC}}$, $\mathcal{F}_{\mathrm{EC}}$, $\mathcal{S}_{\mathrm{PD}}$, and $\mathcal{S}_{\mathrm{EC}}$ operate along a northern trajectory that tracks a Flower Tc state that formed north-east of Barbados on February 2-3, 2020 [Narenpitak et al., 2021], during the ATOMIC [Pincus et al., 2021] and EUREC^{4}A [Stevens et al., 2021] field campaigns. The simulations $\mathcal{F}^{*}_{\mathrm{PD}}$, $\mathcal{F}^{*}_{\mathrm{EC}}$, $\mathcal{F}^{**}_{\mathrm{PD}}$, and $\mathcal{F}^{**}_{\mathrm{EC}}$ operate along a southern trajectory, which captures different conditions on the same day, with a warmer sea surface temperature, a lower estimated inversion strength, and an initally faster wind speed (Fig. SF2). The trajectories were determined from the wind field at 500 m of the fifth generation of the European Centre for Medium-Range Weather Forecasts (ECMWF) atmospheric reanalysis [ERA5, Hersbach et al., 2020] using the Hybrid Single Particle Lagrangian Integrated Trajectory Model [HYSPLIT, Stein et al., 2015].

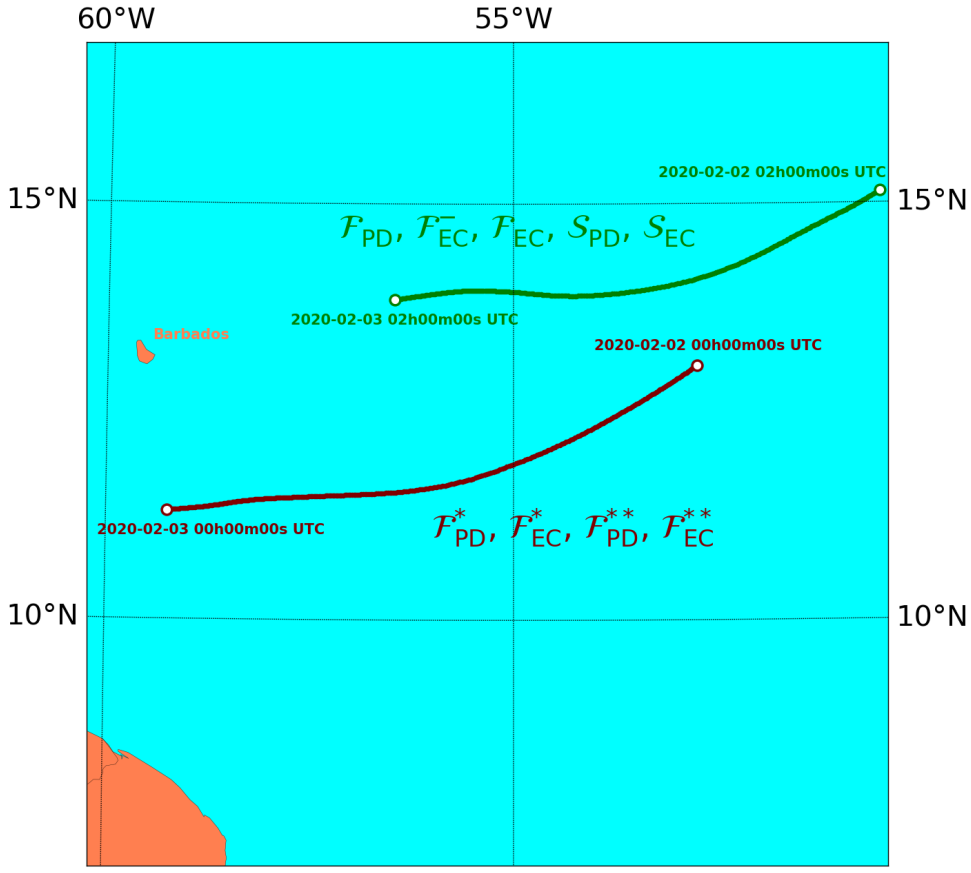

Figure SF1: Simulation trajectories. The northern trajectory runs from 15.14° N, 50.44° W to 13.85° N, 56.41° W. The southern trajectory runs from 13.05° N, 52.74° W to 11.30° N, 59.20° W.

Simulations along the northern trajectory use a 192 km × 192 km domain, simulations along the southern trajectory a 96 km × 96 km domain, and all simulations extend from the surface to 10 km. The smaller domain of the southern simulations allows sensitivity tests with a finer vertical grid spacing. The simulation use periodic

lateral boundary conditions. The horizontal grid spacing is 100 m, the default vertical grid spacing 50 m from the surface to 5000 m, followed by 25 geometric levels up to domain top. For sensitivity tests, the vertical grid spacing is refined to 25 m in the cloud layer, between 700 m and 5000 m, followed by 30 geometric levels up to domain top, in select simulations along the southern trajectory. The simulation time step is 2 s in all simulations. Table ST1 gives mean values over the 24 h duration of the simulations. Key parameters of the simulations are listed in Table ST2 and ST3, respectively.

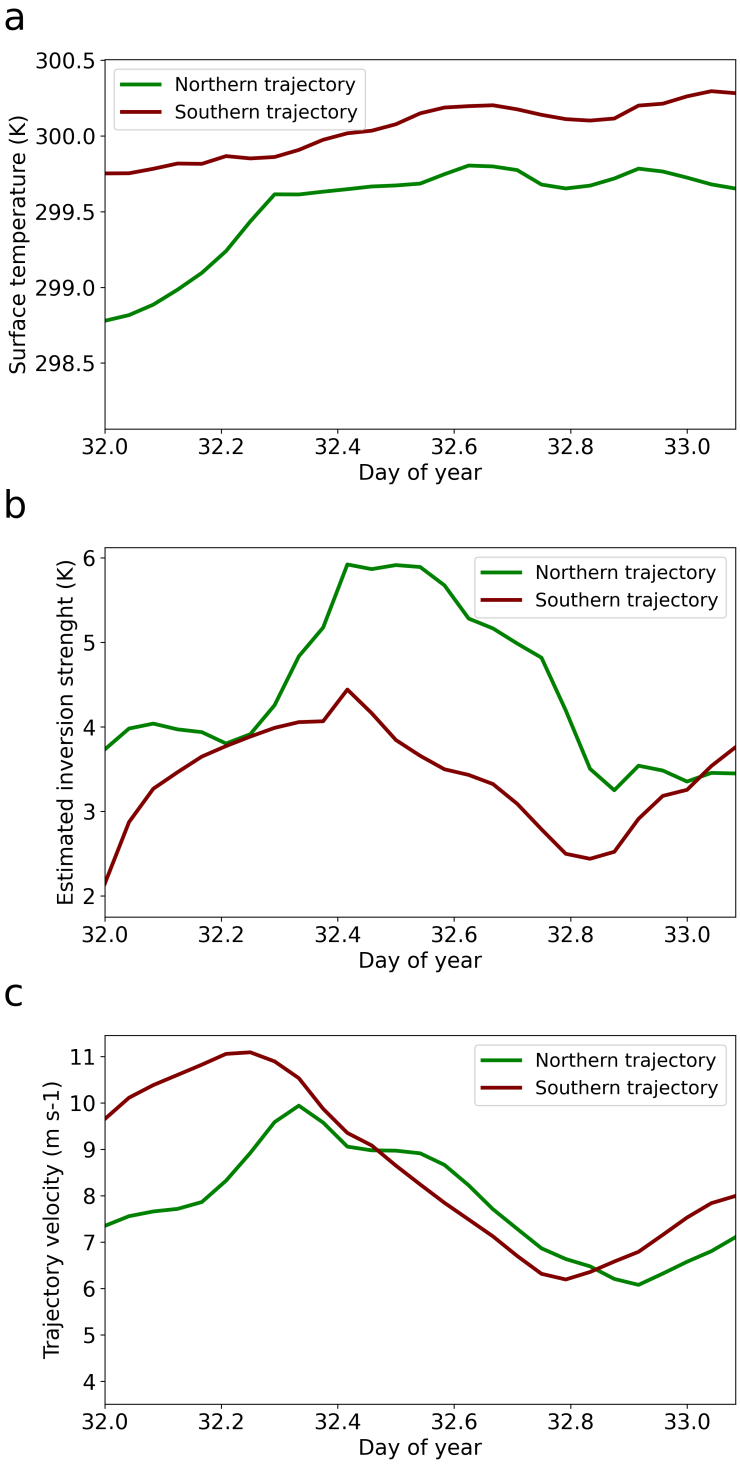

Figure SF2: Select PD conditions from the ERA5 reanalysis along the simulation trajectories: (a) sea surface temperature, (b) estimated inversion strength, and (c) trajectory velocity. The trajectory velocity is the wind speed at 500 m above the surface.

	CF	LWP ($g\,m^{-2}$)	SWCRE ($W\,m^{-2}$)
$\mathcal{F}_{PD}$	0.085	11.7	-14.8
$\mathcal{F}^{-}_{EC}$	0.083	10.9	-14.3
$\mathcal{F}_{EC}$	0.078	9.0	-13.5
$\mathcal{S}_{PD}$	0.077	8.9	-10.4
$\mathcal{S}_{EC}$	0.073	7.9	-10.0
$\mathcal{F}^{*}_{PD}$	0.088	19.1	-15.2
$\mathcal{F}^{**}_{PD}$	0.096	23.6	-17.2
$\mathcal{F}^{*}_{EC}$	0.079	14.9	-13.5
$\mathcal{F}^{**}_{EC}$	0.085	17.9	-14.2

Table ST1: Mean values over the 24 h duration of the simulations of cloud fraction (CF), liquid water path (LWP), and short-wave cloud radiative effect (SWCRE).

The sea surface temperature (SST), large scale meteorology (LSM), and GHG forcing our simulations were obtained from ERA5 along the simulation trajectories, and from the three ensemble members r2i1p1, r3i1p1, and r4i1p1 [National Science Foundation; US Department of Energy; National Center for Atmospheric Research, 2017] of the Coupled Model Intercomparison Project Phase 5 [CMIP5, Taylor et al., 2012] RCP8.5 scenario simulated with the first version of the Community Earth System Model - Whole Atmosphere Community Climate Model [CESM1(WACCM), Marsh et al., 2013]. LSM consists of atmospheric temperature, water vapor, zonal and meridional wind speed, and subsidence, GHG species are CO_2, CH_4, N_2O, and O_3.

We averaged the CESM1(WACCM) RCP8.5 simulation ensemble for January and February over the region 10–22° N, 295–310° E, which spans the simulation trajectories, over 2016–2025 to represent present-day (PD) conditions, and over 2090–2099 to represent end-of-21st-century (EC) conditions. The temporal averaging suppresses interannual variability. The forcing of our simulations in PD conditions consists of the ERA5 SST and LSM together with the CO_2, CH_4, N_2O, and O_3 profiles in the CESM1(WACCM) RCP8.5 simulation ensemble averaged over the specified region and the PD time period. The forcing of our simulations in EC conditions is constructed from the PD forcing by adding the change in SST, LSM, and GHG from the PD period to EC period in the CESM1(WACCM) RCP8.5 simulation ensemble, averaged over the specified region. The EC and PD forcings also provide temperature, water vapor, and GHG profiles above model top for the radiation calculation. The PD and EC GHG profiles are displayed in Fig. SF3, the PD and EC LSM profiles in Fig. SF4.

At the 500 m height of the simulation trajectories, the difference in horizontal wind speed from PD to EC in CESM1(WACCM) is approximately 0.1 $m\,s^{-1}$, resulting in a shift by about 11 km in trajectory end location over the 24 h simulations. We ignore this shift and use the PD trajectories for all simulations.

Fig. SF6 shows the LSM in PD to EC under the RCP8.5 scenario in the region 10–22° N, 295–310° E across select CMIP5 models. These models include HadGEM-2A, MIROC5, and CCSM4, which reasonably reproduce observations in the shallow cumulus cloud regime relative to other CMIP5 models [Nam et al., 2012], and CESM1-CAM5, which uses CESM1 as in CESM1-WACCM. LSM changes consistently across models from EC to PD. Water vapor increases only in the boundary layer in each model. Temperature increases by a larger value in the mid- to upper troposphere compared to the surface, corresponding to an increase in tropospheric stability across the models. Vertical pressure velocity (subsidence) changes negligibly below 875 mbar (approximately 1200 m), and weakens in the troposphere above. The sole outlier is the meridional wind speed (V) in CESM1-CAM5 and HadGem2-ES, which turns more southerly from PD to EC. Overall, the change in LSM from PD to EC in CESM1-WACCM is broadly representative of the CMIP5 models which reasonably reproduce observations in the shallow cumulus cloud regime.

Simulation	$\mathcal{F}_{\mathrm{PD}}$	$\mathcal{F}_{\mathrm{EC}}^{-}$	$\mathcal{F}_{\mathrm{EC}}$	$\mathcal{S}_{\mathrm{PD}}$	$\mathcal{S}_{\mathrm{EC}}$
Cloud type	Flowers	Flowers	Flowers	Sugar	Sugar
Mean SST	299.6 K	301.4 K	301.4 K	299.6 K	301.4 K
GHG levels	2016-2025	2016-2025	2090-2099	2016-2025	2090-2099
Meteorological forcing	ERA5	ERA5 + $\Delta_{\mathrm{PD}\to\mathrm{EC}}$RCP8.5	ERA5 + $\Delta_{\mathrm{PD}\to\mathrm{EC}}$RCP8.5	ERA5	ERA5 + $\Delta_{\mathrm{PD}\to\mathrm{EC}}$RCP8.5
Notes				Large scale subsidence profile held constant from 10h00m UTC on February 2.	

Table ST2: Parameters of simulations along northern trajectory. The term $\Delta_{\mathrm{PD}\to\mathrm{EC}}$RCP8.5 represents the change in the forcing from present-day (PD) to end-of-21st-century (EC) conditions.

The simulations are initialized with temperature and water vapor profiles from the forcing data at the start of the trajectory. The simulations are nudged towards the LSM using Newtonian relaxation. Horizontal mean temperature and water vapor are nudged only in the free troposphere, mean horizontal wind speed is nudged at all altitudes [Kazil et al., 2021]. Subsidence from the LSM forcing is prescribed in the simulations (Fig. SF5). Aerosol is initialized with measurements from the ATOMIC field campaign [Narenpitak et al., 2021]. For generality, we ignore a free-tropospheric mineral dust layer observed during several days in the ATOMIC and EUREC^{4}A field campaigns [Narenpitak et al., 2021]. The Sugar simulations are constructed from the Flower simulations by holding the subsidence profile constant starting from 8 h into the simulations (Fig. SF5c, d). This suppresses large scale upward motion and keeps the cloud field in the Sugar Tc state until sunset. The role of large scale vertical motion on the evolution of the Flower Tc state is discussed in [Narenpitak et al., 2021].

Simulation	$\mathcal{F}_{\mathrm{PD}}^{*}$	$\mathcal{F}_{\mathrm{EC}}^{*}$	$\mathcal{F}_{\mathrm{PD}}^{**}$	$\mathcal{F}_{\mathrm{EC}}^{**}$
Cloud type	Flowers	Flowers	Flowers	Flowers
Mean SST	300.0 K	301.8 K	300.0 K	301.8 K
GHG levels	2016-2025	2090-2099	2016-2025	2090-2099
Meteorological forcing	ERA5	ERA5 + $\Delta_{\mathrm{PD}\to\mathrm{EC}}$RCP8.5	ERA5	ERA5 + $\Delta_{\mathrm{PD}\to\mathrm{EC}}$RCP8.5
Notes			dz = 25 m from 700 m to 5000 m	dz = 25 m from 700 m to 5000 m

Table ST3: Parameters of simulations along southern trajectory. The term $\Delta_{\mathrm{PD}\to\mathrm{EC}}$RCP8.5 represents the change in the forcing from present-day (PD) to end-of-21st-century (EC) conditions. Simulation $\mathcal{F}_{\mathrm{PD}}^{**}$ and $\mathcal{F}_{\mathrm{EC}}^{**}$ use a vertical grid spacing refined from 50 to 25 m in from the top of the mixed layer ($\sim$700 m) to 5000 m. In the mixed layer, the grid spacing is not refined in order to maintain the numerical treatment of vertical fluxes across the mixed layer.

2 Present-day (PD) and end-of-21st-century (EC) large scale conditions

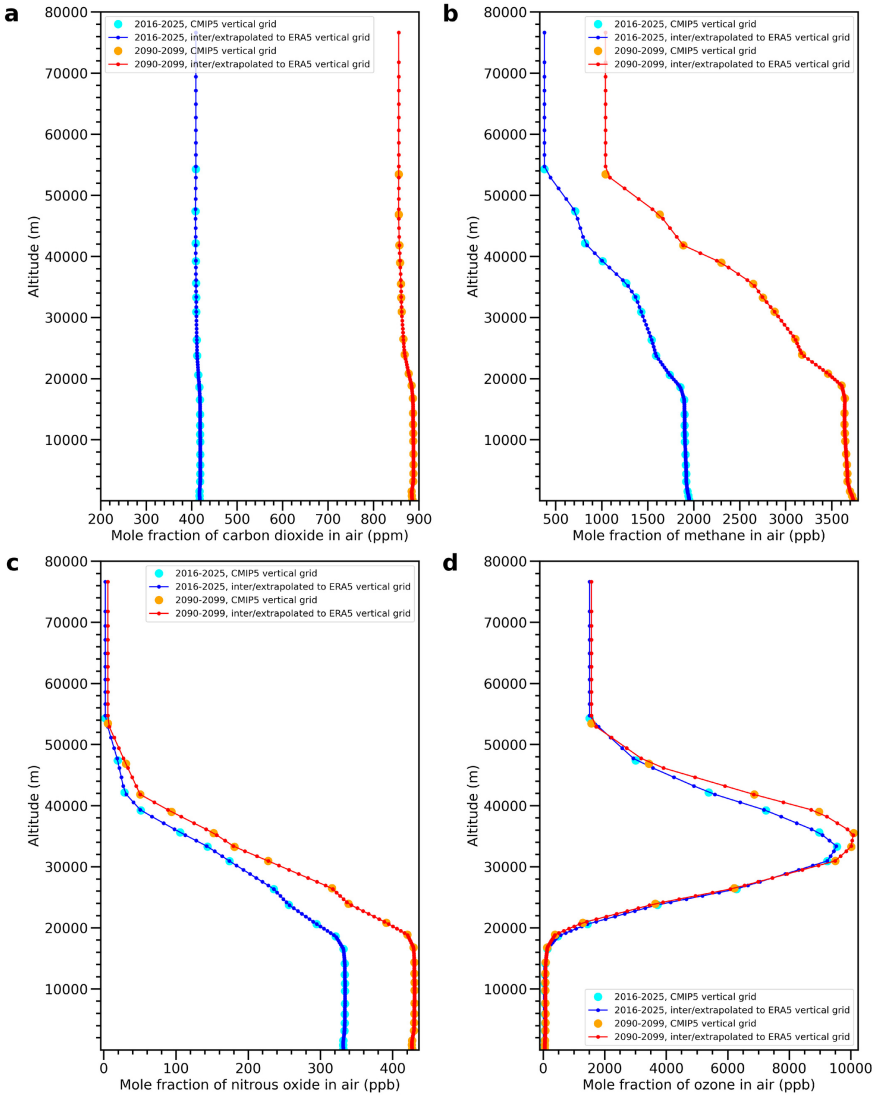

Figure SF3: PD and EC trace gas concentrations: (a) carbon dioxide (CO_2), (b) methane (CH_4), nitrous oxide (N_2O), and ozone (O_3). The profiles were obtained by averaging the monthly-mean output from the three ensemble members r2i1p1, r3i1p1, and r4i1p1 [National Science Foundation; US Department of Energy; National Center for Atmospheric Research, 2017] of the Coupled Model Intercomparison Project 5 [CMIP5 Taylor et al., 2012] RCP8.5 scenario simulations with the first version of the Community Earth System Model - Whole Atmosphere Community Climate Model CESM1(WACCM) [Marsh et al., 2013] in the years 2016–2025 (PD) and 2090–2099 (EC) over the region 10–22° N, 295–310° E, the Caribbean east of Barbados. The CESM1(WACCM) data were interpolated to the fifth generation of the European Centre for Medium-Range Weather Forecasts (ECMWF) atmospheric reanalysis [ERA5, Hersbach et al., 2020] vertical grid, on which the forcing data for the simulations are defined. CESM1(WACCM) output is available up to an altitude of approximately 54 km. Forcing data at higher altitudes on the ERA5 grid, which extends to approximately 80 km were populated with the top-level CESM1(WACCM) values.

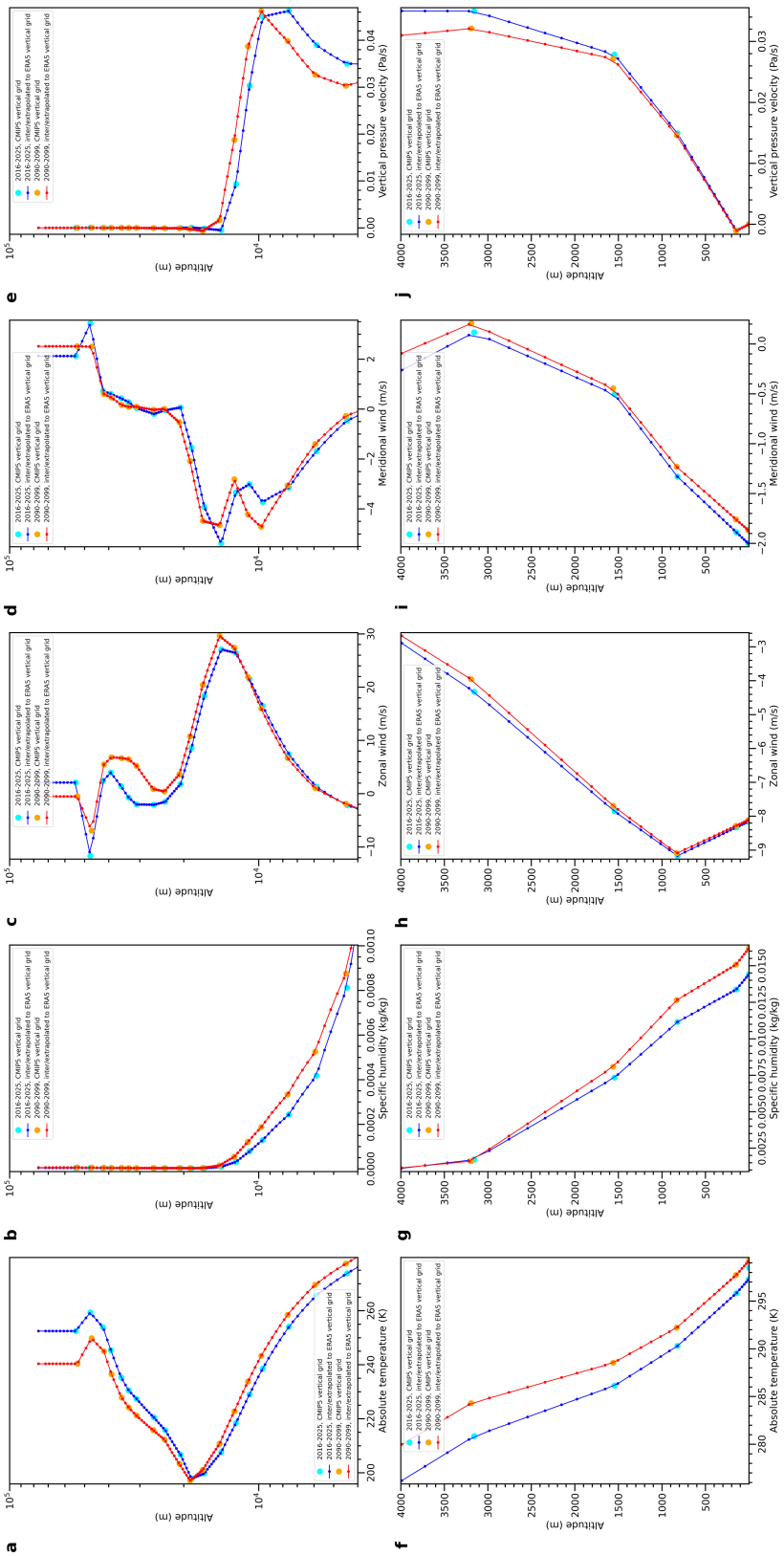

Figure SF4: CMIP5 RCP8.5 PD and EC meteorology (a–e) above and (f–j) below 4000 m: (a, f) temperature, (b, g) specific humidity, (c, h) zonal wind, (d, i) meridional wind, and (e, j) vertical pressure velocity (subsidence). The profiles were obtained by averaging the monthly-mean output from the three ensemble members r2i1p1, r3i1p1, and r4i1p1 [National Science Foundation; US Department of Energy; National Center for Atmospheric Research, 2017] of the Coupled Model Intercomparison Project 5 [CMIP5 Taylor et al., 2012] RCP8.5 scenario simulations with the first version of the Community Earth System Model - Whole Atmosphere Community Climate Model CESM1(WACCM) [Marsh et al., 2013] in the years 2016–2025 (PD) and 2090–2099 (EC) over the region 10–22° N, 295–310° E, the Caribbean east of Barbados. The CESM1(WACCM) data were interpolated to the fifth generation of the European Centre for Medium-Range Weather Forecasts (ECMWF) atmospheric reanalysis [ERA5, Hersbach et al., 2020] vertical grid, on which the forcing data for the simulations are defined. CESM1(WACCM) output is available up to an altitude of approximately 54 km. Forcing data at higher altitudes on the ERA5 grid, which extends to approximately 80 km were populated with the top-level CESM1(WACCM) values. The difference EC-PD is added to the PD forcing to obtain the EC forcing.

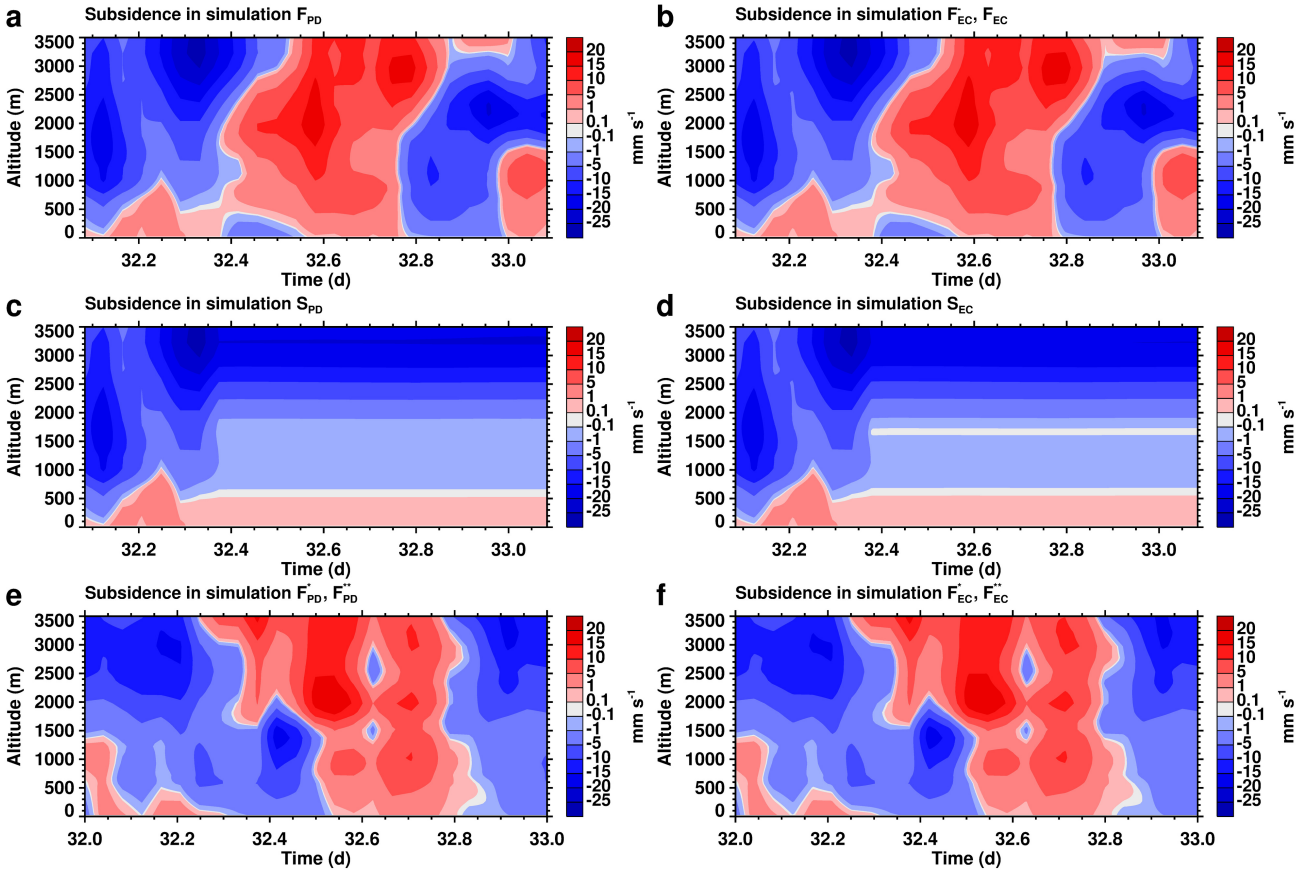

Figure SF5: Prescribed subsidence profiles in simulation (a) $\mathcal{F}_{\mathrm{PD}}$, (b) $\mathcal{F}^{-}_{\mathrm{EC}}$ and $\mathcal{F}_{\mathrm{EC}}$, (c) $\mathcal{S}_{\mathrm{PD}}$, (d) $\mathcal{S}_{\mathrm{EC}}$, (e) $\mathcal{F}^{*}_{\mathrm{PD}}$ and $\mathcal{F}^{**}_{\mathrm{PD}}$, and (f) $\mathcal{F}^{*}_{\mathrm{EC}}$ and $\mathcal{F}^{**}_{\mathrm{EC}}$.

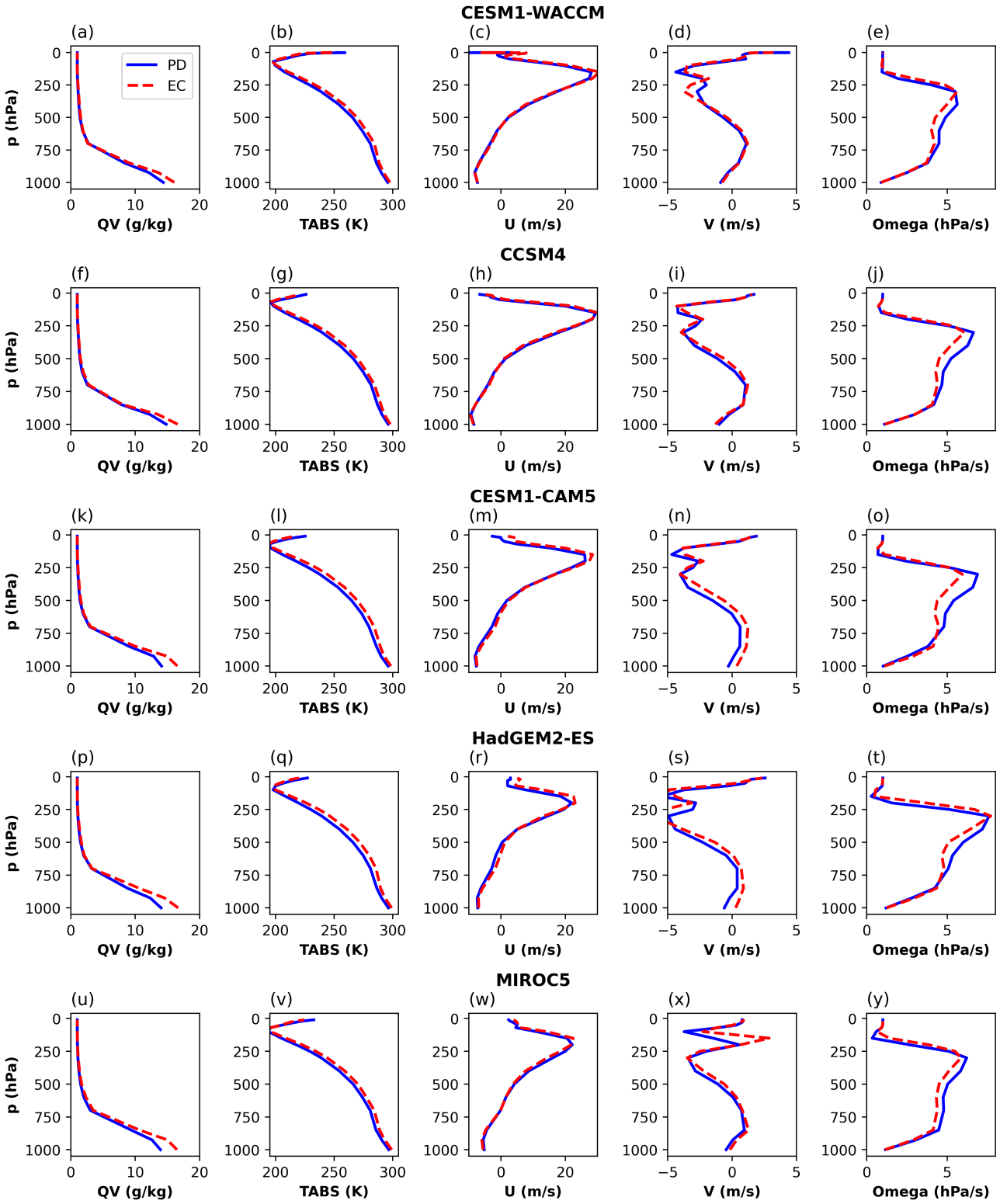

Figure SF6: Large scale meteorology (LSM) in the CMIP5 RCP8.5 scenario, averaged for January and February over the region 10–22° N, 295–310° E, over 2016–2025, representing PD conditions (blue), and 2090–2099, representing EC conditions (red). (a-e) CESM1(WACCM) ensemble r2i1p1 through r4i1p1, used in this work; (f-j) CCSM4 ensemble r1i1p1 through r3i1p1; (k-o) CESM1-CAM5 ensemble r1i1p1 through r3i1p1; (p-t) HadGEM2-ES ensemble r1i1p1 through r4i1p1; (u-y) MIROC ensemble r1i1p1 through r3i1p1.

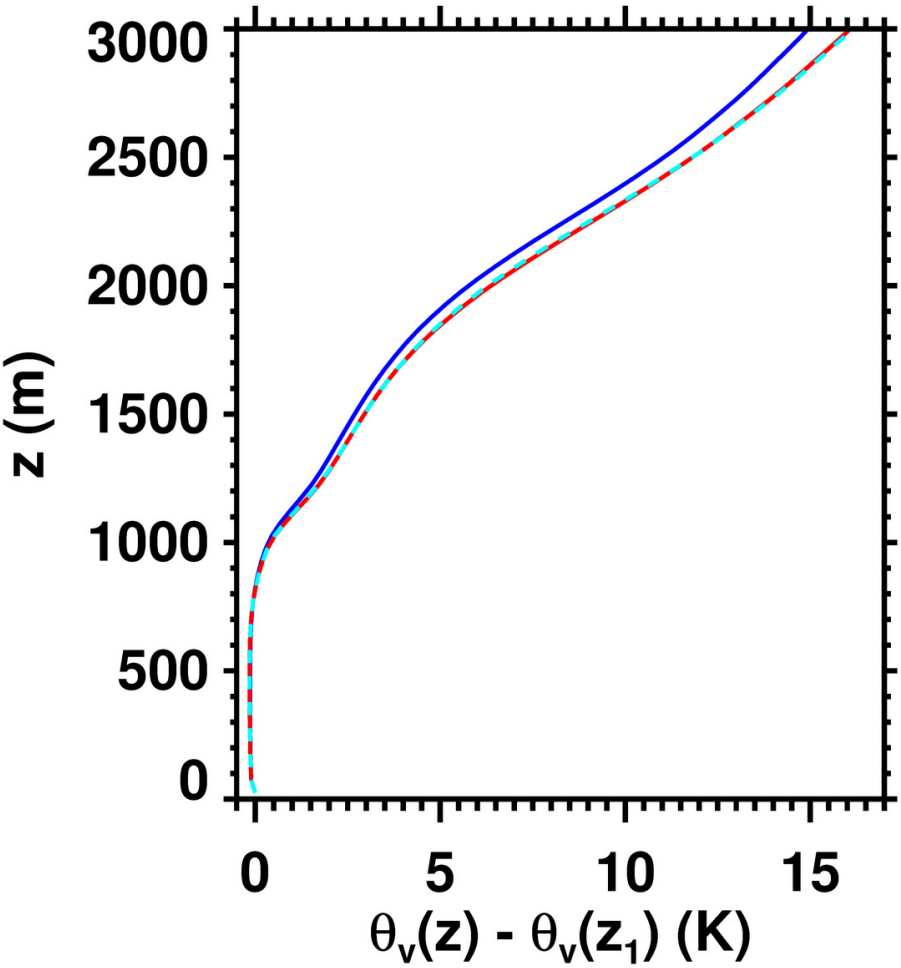

Figure SF7: Atmospheric stability in the simulation $\mathcal{F}_{\mathrm{PD}}$ (blue), $\mathcal{F}_{\mathrm{EC}}^{-}$ (cyan) and $\mathcal{F}_{\mathrm{EC}}$ (red). Stability is diagnosed as the difference of virtual potential temperature $\theta_v(z) - \theta_v(z_1)$, where z_1 is the lowermost model level. The average over the 24 h duration of the simulations is shown.

3 Mean base of active cloud convection (BACC)

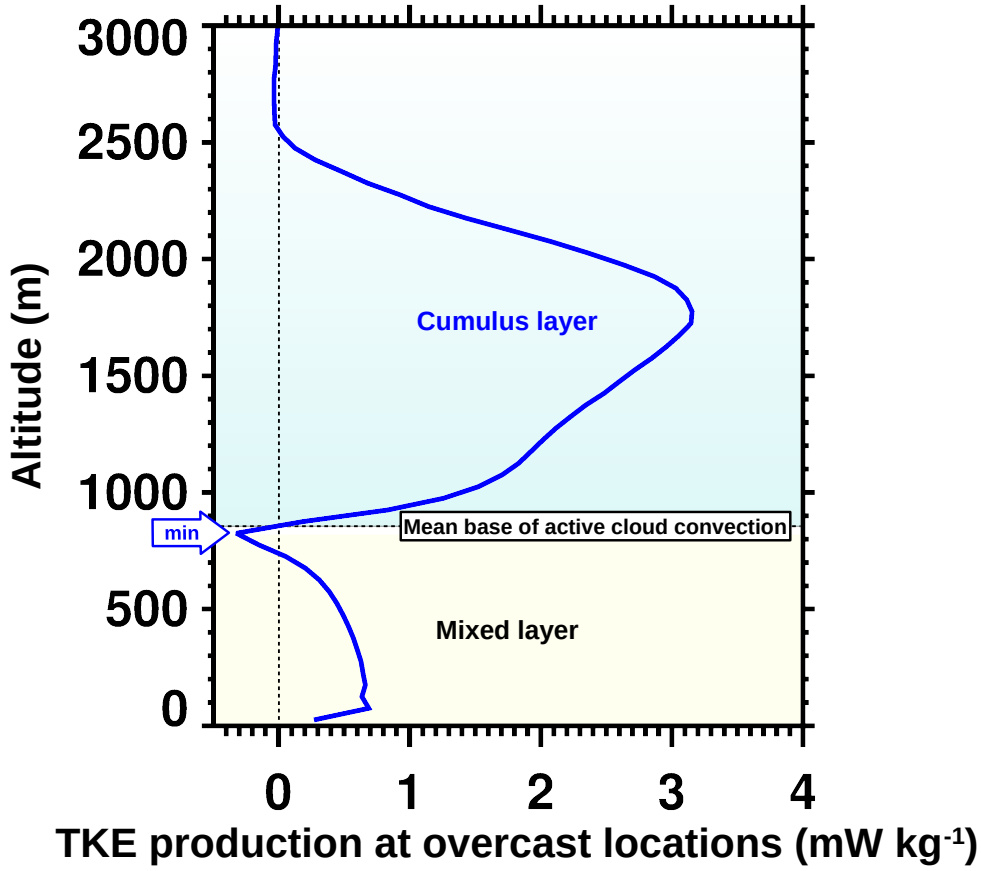

Figure SF8: The mean base of active cloud convection (BACC) is diagnosed from the average profile of TKE production due to buoyancy at overcast locations (locations with a liquid water path $\geq 0.1\,\mathrm{g\,m^{-2}}$). It is the location at which the profile first reaches or exceeds 0 above the altitude where the TKE production profile has a minimum.

4 Additional results of simulation $\mathcal{F}_{\mathrm{PD}}$, $\mathcal{F}_{\mathrm{EC}}^{-}$, $\mathcal{F}_{\mathrm{EC}}$, $\mathcal{S}_{\mathrm{PD}}$ and $\mathcal{S}_{\mathrm{EC}}$

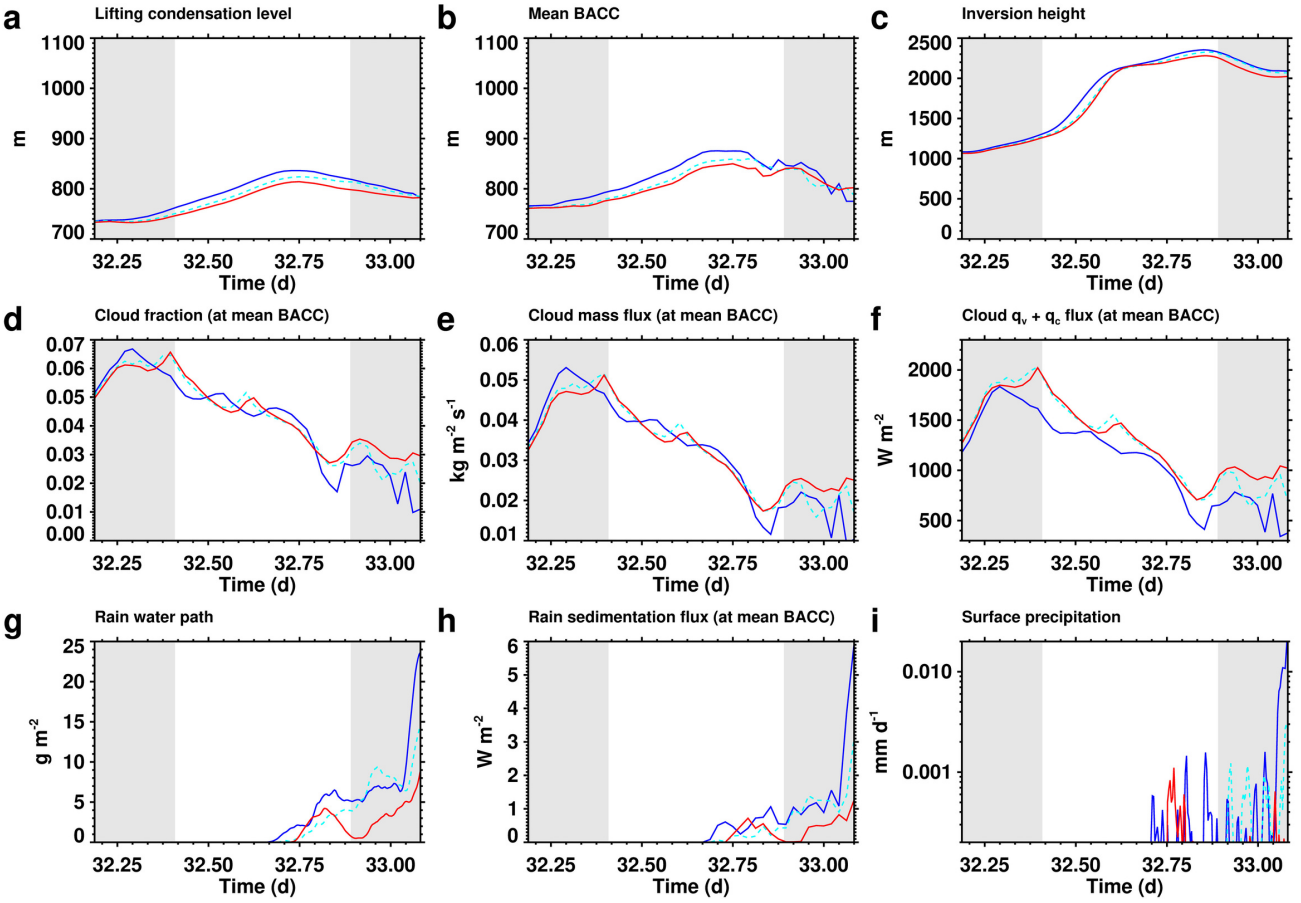

Figure SF9: Time series from the simulation $\mathcal{F}_{\mathrm{PD}}$ (blue), $\mathcal{F}_{\mathrm{EC}}^{-}$ (cyan) and $\mathcal{F}_{\mathrm{EC}}$ (red): (a) lifting condensation level, calculated as a domain average of the local lifting condensation level using Eq. (22) in Bolton [1980], (b) mean base of active cloud convection (BACC), (c) inversion height, (d) cloud fraction at mean BACC, (e) cloud mass flux at mean BACC, (f) sum of the water vapor and cloud water flux at mean BACC, (g) rain water path, (h) rain water mass sedimentation flux at mean BACC, and (i) surface precipitation. Shading indicates nighttime.

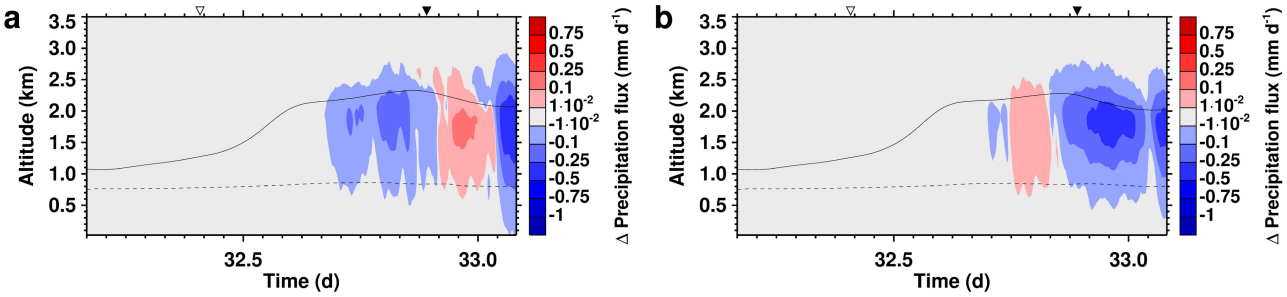

Figure SF10: Change in precipitation flux from (a) $\mathcal{F}_{\mathrm{PD}}$ to $\mathcal{F}_{\mathrm{EC}}^{-}$ and from (b) $\mathcal{F}_{\mathrm{EC}}^{-}$ to $\mathcal{F}_{\mathrm{EC}}$. An open triangle marks sunrise, a solid triangle sunset. The mean base of active cloud convection (BACC) is drawn as a dashed curve, the inversion height as a solid curve.

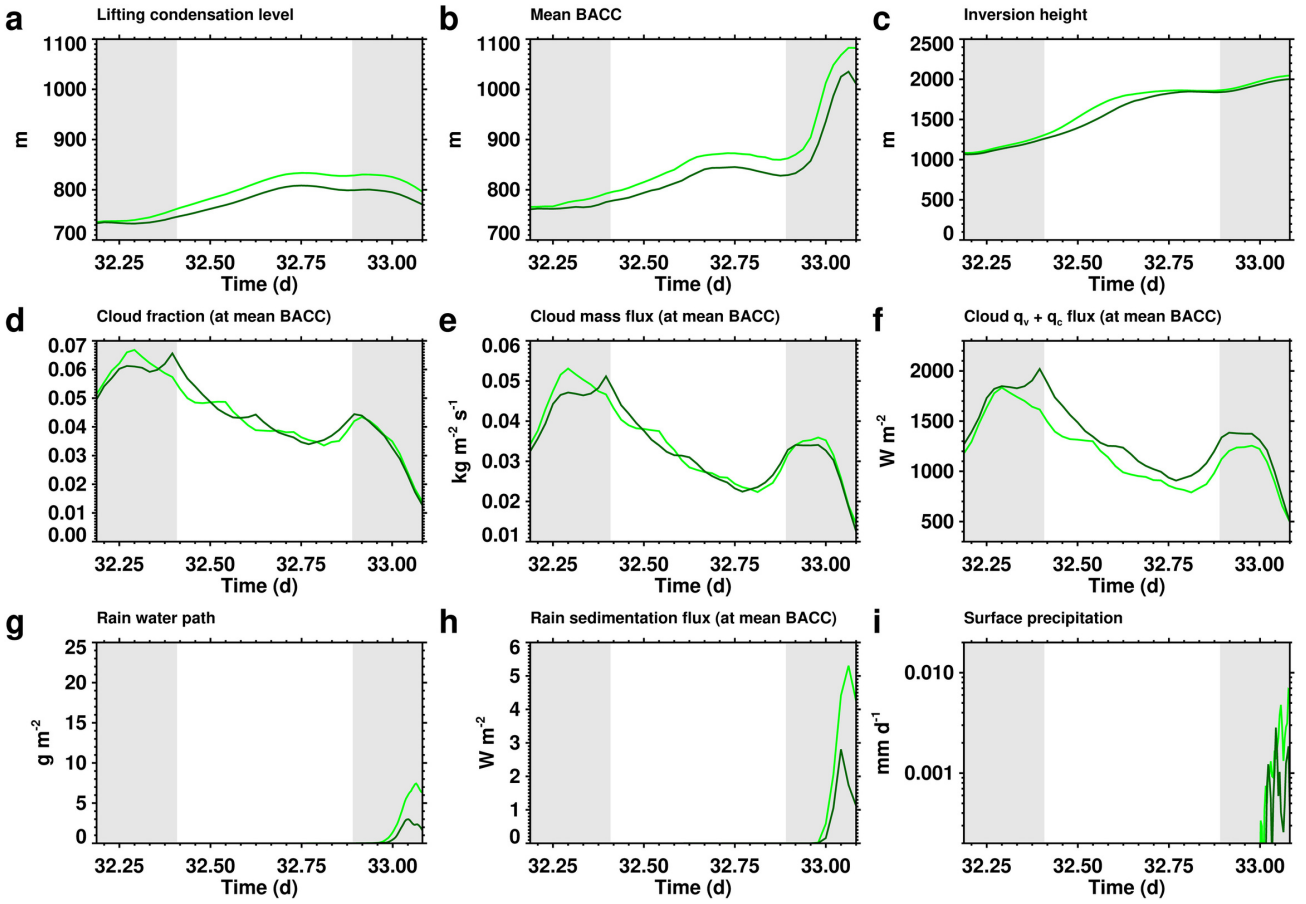

Figure SF11: Time series from the simulation $\mathcal{S}_{\mathrm{PD}}$ (light green) and $\mathcal{S}_{\mathrm{EC}}$ (dark green): (a) lifting condensation level, calculated as a domain average of the local lifting condensation level using Eq. (22) in Bolton [1980], (b) mean base of active cloud convection (BACC), (c) inversion height, (d) cloud fraction at mean BACC, (e) cloud mass flux at mean BACC, (f) sum of the water vapor and cloud water flux at mean BACC, (g) rain water path, (h) rain water mass sedimentation flux at mean BACC, and (i) surface precipitation. Shading indicates nighttime.

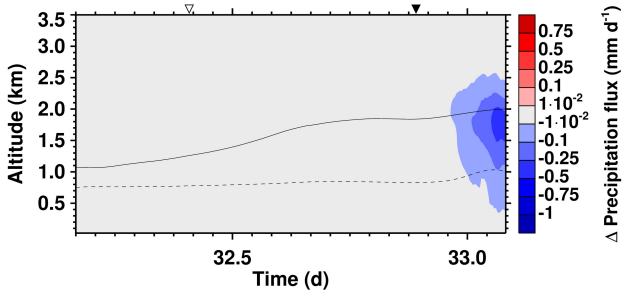

Figure SF12: Change in precipitation flux from $\mathcal{S}_{\mathrm{PD}}$ to $\mathcal{S}_{\mathrm{EC}}$. An open triangle marks sunrise, a solid triangle sunset. The mean base of active cloud convection (BACC) is drawn as a dashed curve, the inversion height as a solid curve.

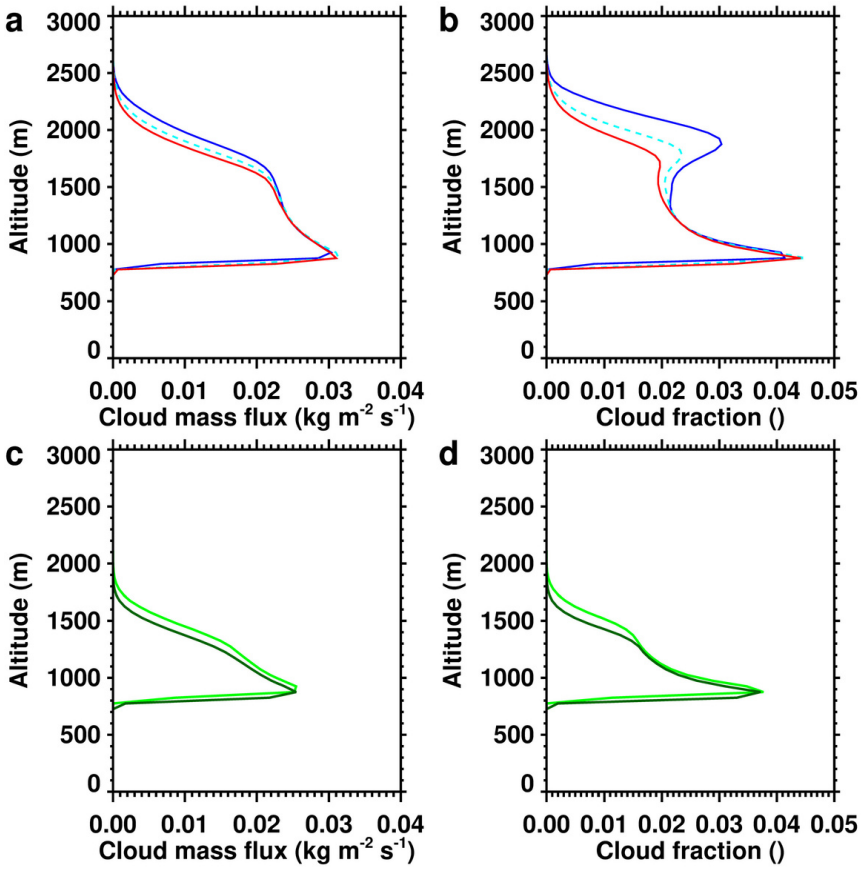

Figure SF13: Cloud mass flux (left column) and cloud fraction (right column) from the simulation $\mathcal{F}_{\rm PD}$ (blue), $\mathcal{F}_{\rm EC}^{-}$ (cyan) and $\mathcal{F}_{\rm EC}$ (red), $\mathcal{S}_{\rm PD}$ (light green), and $\mathcal{S}_{\rm EC}$ (dark green), at 18h00 UTC (d = 32.75).

5 Radiative heating analysis in simulation $\mathcal{F}_{\mathrm{PD}}$, $\mathcal{F}_{\mathrm{EC}}^{-}$, and $\mathcal{F}_{\mathrm{EC}}$

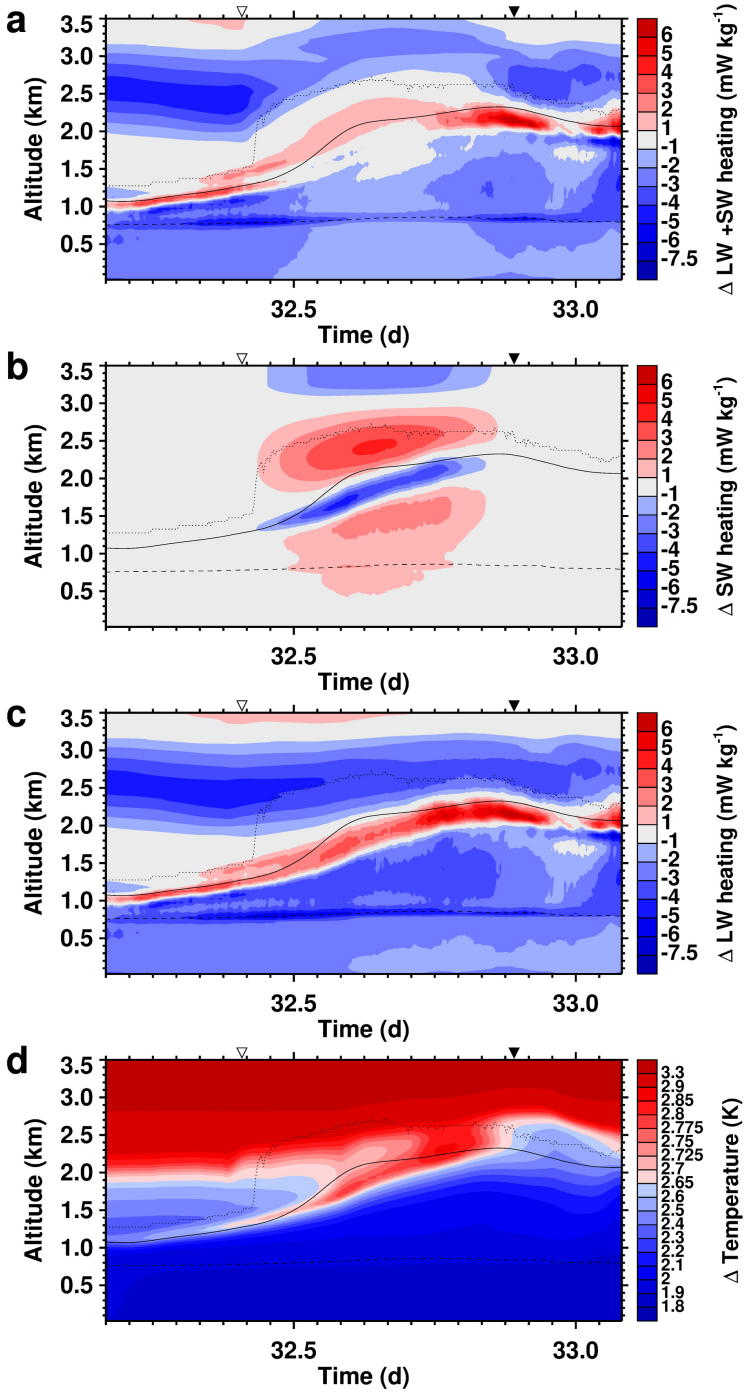

Figure SF14: Change from simulation $\mathcal{F}_{\mathrm{PD}}$ to $\mathcal{F}_{\mathrm{EC}}^{-}$ in (a) radiative heating, (b) short-wave, and (c) long-wave heating, and (d) the change in temperature from $\mathcal{F}_{\mathrm{PD}}$ to $\mathcal{F}_{\mathrm{EC}}^{-}$. Non-constant contour intervals are used in (d) to isolate the temperature change structure at the inversion. The mean base of active cloud convection (BACC) is drawn as a dashed curve, the inversion height as a solid curve. The nudging base height (dotted) is the altitude above which temperature and water vapor are nudged towards the forcing profiles. The peak in the radiative heating change (a) and the resulting temperature response (d) around the inversion are located below the nudging base height. An open triangle marks sunrise, a solid triangle sunset.

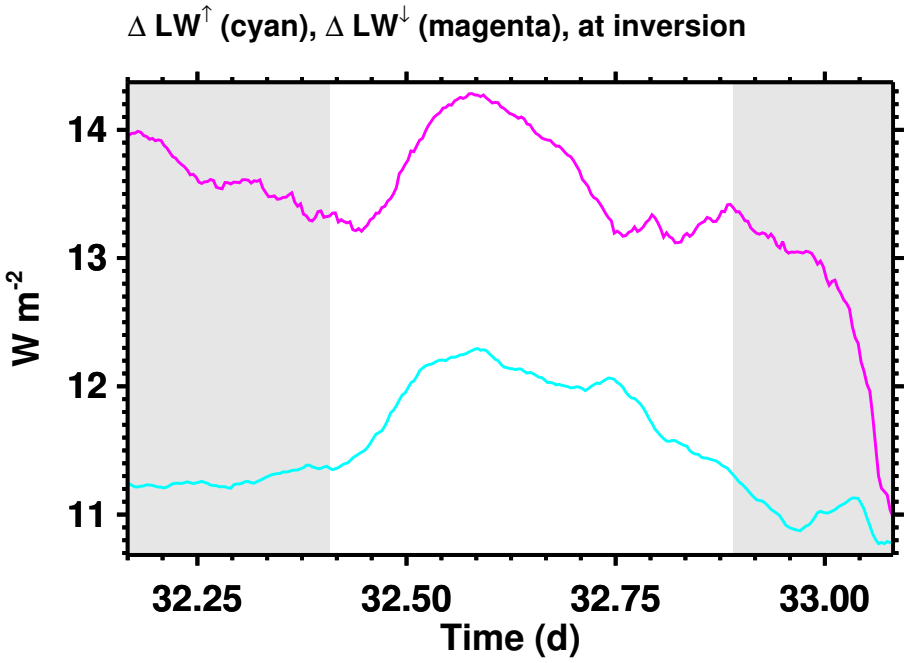

Figure SF15: Change from simulation $\mathcal{F}_{\mathrm{PD}}$ to $\mathcal{F}^{-}_{\mathrm{EC}}$ at the inversion of $\mathcal{F}^{-}_{\mathrm{EC}}$ in up-welling (cyan) and down-welling (magenta) longwave radiation.

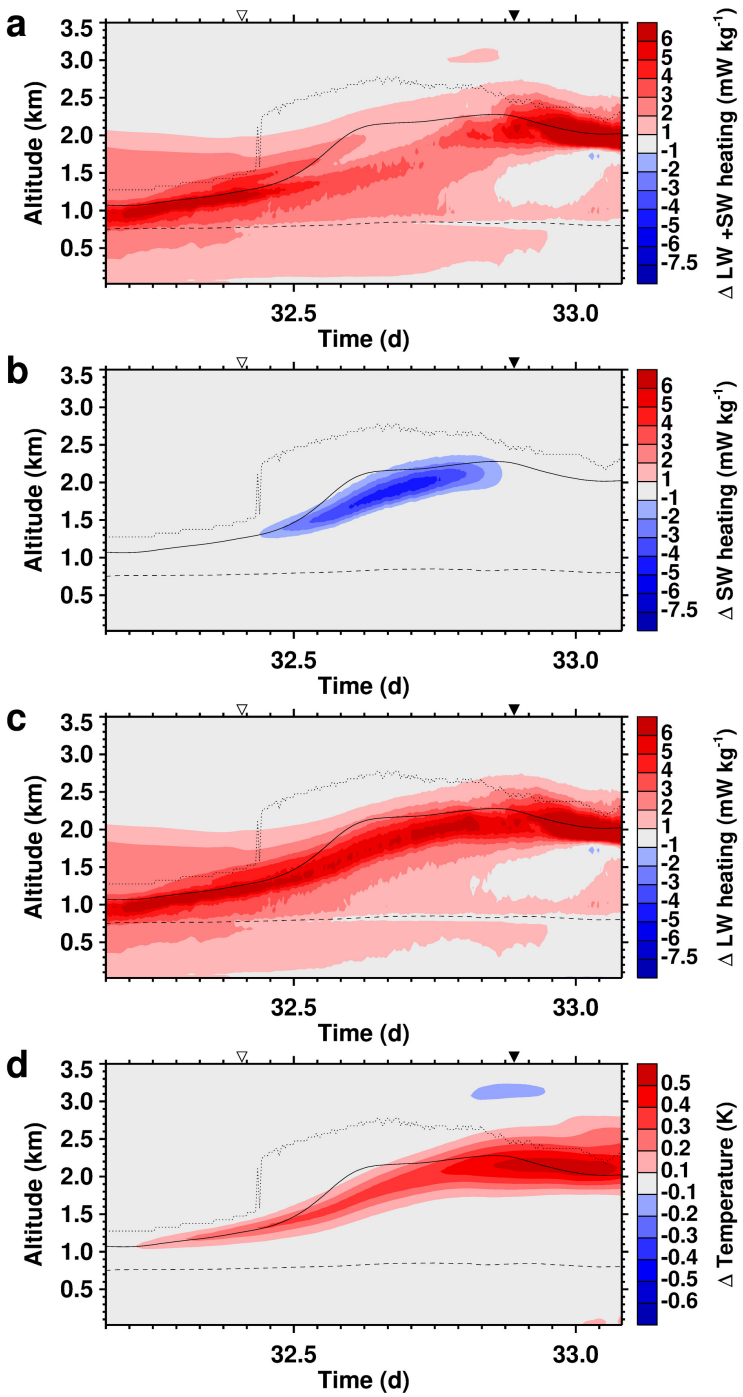

Figure SF16: Change from simulation $\mathcal{F}_{\mathrm{EC}}^{-}$ to $\mathcal{F}_{\mathrm{EC}}$ in (a) radiative heating, (b) short-wave, and (c) long-wave heating, and (d) the change in temperature from $\mathcal{F}_{\mathrm{EC}}^{-}$ to $\mathcal{F}_{\mathrm{EC}}$. The mean base of active cloud convection (BACC) is drawn as a dashed curve, the inversion height as a solid curve. The nudging base height (dotted) is the altitude above which temperature and water vapor are nudged towards the forcing profiles. The peak in the radiative heating change (a) and the resulting temperature response (d) around the inversion are located below the nudging base height. An open triangle marks sunrise, a solid triangle sunset.

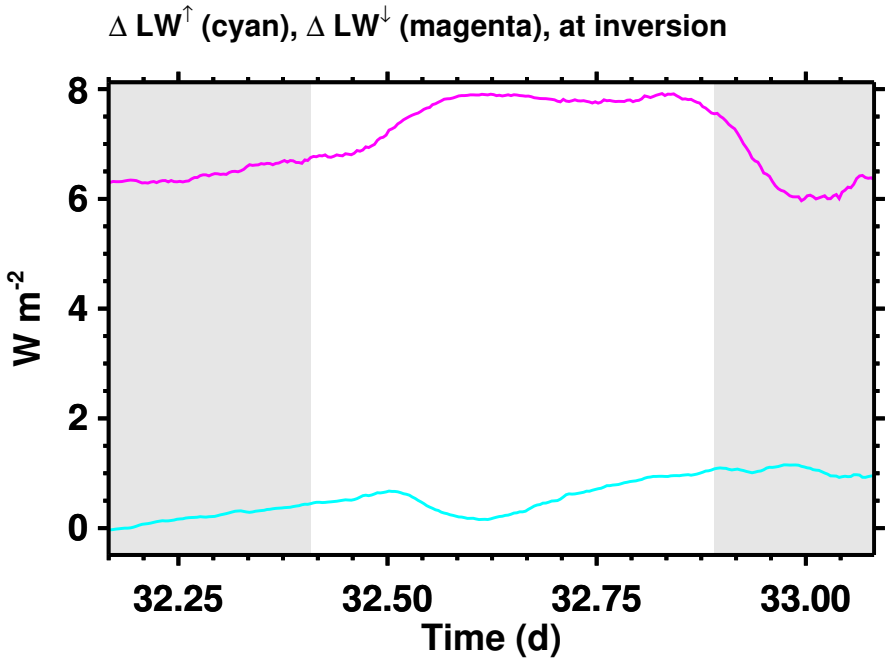

Figure SF17: Change from simulation $\mathcal{F}_{\mathrm{EC}}^{-}$ to $\mathcal{F}_{\mathrm{EC}}$ at the inversion of $\mathcal{F}_{\mathrm{EC}}$ at the inversion in up-welling (cyan) and down-welling (magenta) longwave radiation.

6 Results of simulation $\mathcal{F}^{*}_{\mathrm{PD}}$, $\mathcal{F}^{*}_{\mathrm{EC}}$, $\mathcal{F}^{**}_{\mathrm{PD}}$, $\mathcal{F}^{**}_{\mathrm{EC}}$

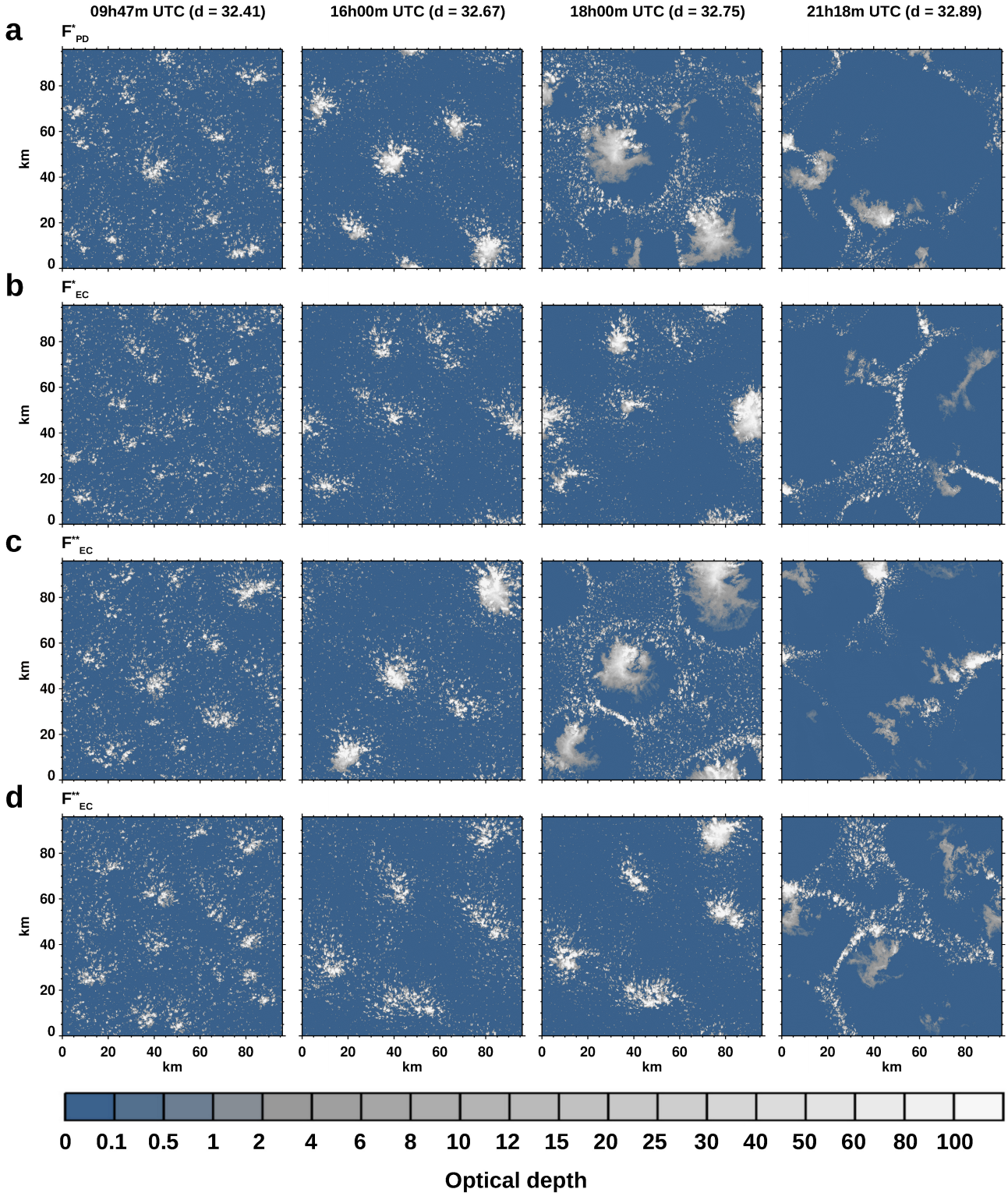

Figure SF18: Trade cumulus evolution in the simulations (a) $\mathcal{F}^{*}_{\mathrm{PD}}$, (b) $\mathcal{F}^{*}_{\mathrm{EC}}$, (c) $\mathcal{F}^{**}_{\mathrm{PD}}$, and (d) $\mathcal{F}^{**}_{\mathrm{EC}}$. Sunrise (first column) is at 09h47m UTC (fractional day of year d = 32.41), sunset (last column) at 21h18m UTC (fractional day of year d = 32.89).

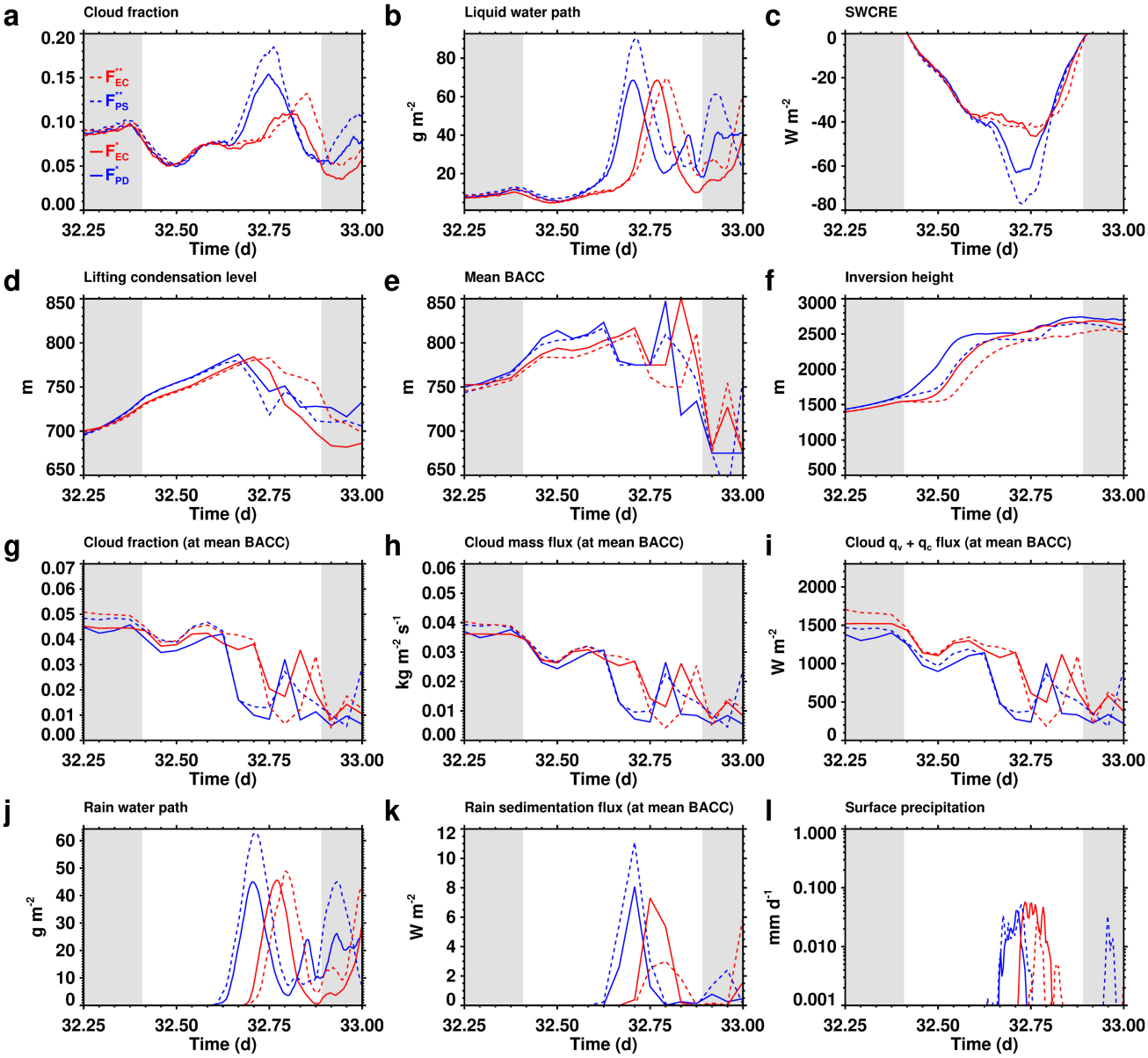

Figure SF19: Time series from the simulation $\mathcal{F}^{*}_{\mathrm{PD}}$ (blue solid), $\mathcal{F}^{**}_{\mathrm{PD}}$ (blue dashed), $\mathcal{F}^{*}_{\mathrm{EC}}$ (red solid), and $\mathcal{F}^{*}_{\mathrm{EC}}$ (red dashed) of (a) short-wave cloud radiative effect, (b) cloud fraction, (c) liquid water path, and (d) surface precipitation (shading indicates nighttime).

References

D. Bolton. The computation of equivalent potential temperature. *Mon. Weather Rev.*, 108(7):1046–1053, 1980. doi: 10.1175/1520-0493(1980)108¡1046:TCOEPT¿2.0.CO;2.

G. Feingold, R. L. Walko, B. Stevens, and W. R. Cotton. Simulations of marine stratocumulus using a new microphysical parameterization scheme. *Atmos. Res.*, 47-48:505–528, 1998. doi: 10.1016/S0169-8095(98)00058-1.

H. Hersbach, B. Bell, P. Berrisford, S. Hirahara, A. Horány, J. Muñoz Sabater, J. Nicolas, C. Peubey, R. Radu, D. Schepers, A. Simmons, C. Soci, S. Abdalla, X. Abellan, G. Balsamo, P. Bechtold, G. Biavati, J. Bidlot, M. Bonavita, G. De Chiara, P. Dahlgren, D. Dee, M. Diamantakis, R. Dragani, J. Flemming, R. Forbes, M. Fuentes, A. Geer, L. Haimberger, S. Healy, R. J. Hogan, E. Hóm, M. Janisková, S. Keeley, P. Laloyaux, P. Lopez, C. Lupu, G. Radnoti, P. de Rosnay, I. Rozum, F. Vamborg, S. Villaume, and J.-N. Thépaut. The ERA5 global reanalysis. *Quarterly Journal of the Royal Meteorological Society*, 146(730):1999–2049, 2020. ISSN 1477-870X. doi: 10.1002/qj.3803.

M. J. Iacono, J. S. Delamere, E. J. Mlawer, M. W. Shephard, S. A. Clough, and W. D. Collins. Radiative forcing by long-lived greenhouse gases: Calculations with the AER radiative transfer models. *J. Geophys. Res.*, 113 (D13103), 2008. doi: 10.1029/2008JD009944.

J. Kazil, M. W. Christensen, S. J. Abel, T. Yamaguchi, and G. Feingold. Realism of lagrangian large eddy simulations driven by reanalysis meteorology: Tracking a pocket of open cells under a biomass burning aerosol layer. *J. Adv. Model. Earth Syst.*, 13(12):e2021MS002664, 2021. doi: 10.1029/2021MS002664.

M. F. Khairoutdinov and D. A. Randall. Cloud resolving modeling of the ARM summer 1997 IOP: Model formulation, results, uncertainties, and sensitivities. *J. Atmos. Sci.*, 60(4):607–625, 2003. doi: 10.1175/1520-0469(2003)060¡0607:CRMOTA¿2.0.CO;2.

Daniel R. Marsh, Michael J. Mills, Douglas E. Kinnison, Jean-Francois Lamarque, Natalia Calvo, and Lorenzo M. Polvani. Climate change from 1850 to 2005 simulated in CESM1(WACCM). *J. Clim.*, 26(19):7372–7391, 2013. doi: 10.1175/JCLI-D-12-00558.1.

E. J. Mlawer, S. J. Taubman, P. D. Brown, M. J. Iacono, and S. A. Clough. Radiative transfer for inhomogeneous atmospheres: RRTM, a validated correlated-k model for the longwave. *J. Geophys. Res.*, 102:16663–16682, 1997. doi: 10.1029/97JD00237.

C. Nam, S. Bony, J.-L. Dufresne, and H. Chepfer. The 'too few, too bright' tropical low-cloud problem in cmip5 models. *Geophys. Res. Lett.*, 39(21):L21801, 2012. doi: 10.1029/2012GL053421.

P. Narenpitak, J. Kazil, T. Yamaguchi, P. Quinn, and G. Feingold. From sugar to flowers: A transition of shallow cumulus organization during ATOMIC. *J. Adv. Model. Earth Syst.*, 13(10):e2021MS002619, 2021. doi: 10.1029/2021MS002619.

National Science Foundation; US Department of Energy; National Center for Atmospheric Research. WCRP CMIP5: The NSF-DOE-NCAR team CESM1-WACCM model output for the rcp85 experiment, 2017. URL `https://catalogue.ceda.ac.uk/uuid/beb9587bd78f4e959869d5c9dbd8a4ce`.

R. Pincus, C. W. Fairall, A. Bailey, H. Chen, P. Y. Chuang, G. de Boer, G. Feingold, D. Henze, Q. T. Kalen, J. Kazil, M. Leandro, A. Lundry, K. Moran, D. A. Naeher, D. Noone, A. J. Patel, S. Pezoa, I. PopStefanija, E. J. Thompson, J. Warnecke, and P. Zuidema. Observations from the NOAA P-3 aircraft during ATOMIC. *Earth Syst. Sci. Data*, 13(7):3281–3296, 2021. doi: 10.5194/essd-13-3281-2021.

A. F. Stein, R. R. Draxler, G. D. Rolph, B. J. B. Stunder, M. D. Cohen, and F. Ngan. NOAA's HYSPLIT Atmospheric Transport and Dispersion Modeling System. *Bulletin of the American Meteorological Society*, 96 (12):2059–2077, 2015. ISSN 0003-0007, 1520-0477. doi: 10.1175/BAMS-D-14-00110.1.

B. Stevens, S. Bony, D. Farrell, F. Ament, A. Blyth, C. Fairall, J. Karstensen, P. K. Quinn, S. Speich, C. Acquistapace, F. Aemisegger, A. L. Albright, H. Bellenger, E. Bodenschatz, K.-A. Caesar, R. Chewitt-Lucas, G. de Boer, J. Delanoë, L. Denby, F. Ewald, B. Fildier, M. Forde, G. George, S. Gross, M. Hagen, A. Hausold, K. J. Heywood, L. Hirsch, M. Jacob, F. Jansen, S. Kinne, D. Klocke, T. Kölling, H. Konow, M. Lothon, W. Mohr, A. K. Naumann, L. Nuijens, L. Olivier, R. Pincus, M. Pöhlker, G. Reverdin, G. Roberts, S. Schnitt, H. Schulz, A. P. Siebesma, C. C. Stephan, P. Sullivan, L. Touzé-Peiffer, J. Vial, R. Vogel, P. Zuidema, N. Alexander, L. Alves, S. Arixi, H. Asmath, G. Bagheri, K. Baier, A. Bailey, D. Baranowski, A. Baron,

S. Barrau, P. A. Barrett, F. Batier, A. Behrendt, A. Bendinger, F. Beucher, S. Bigorre, E. Blades, P. Blossey, O. Bock, S. Böing, P. Bosser, D. Bourras, P. Bouruet-Aubertot, K. Bower, P. Branellec, H. Branger, M. Brennek, A. Brewer, P.-E. Brilouet, B. Brügmann, S. A. Buehler, E. Burke, R. Burton, R. Calmer, J.-C. Canonici, X. Carton, G. Cato Jr., J. A. Charles, P. Chazette, Y. Chen, M. T. Chilinski, T. Choularton, P. Chuang, S. Clarke, H. Coe, C. Cornet, P. Coutris, F. Couvreux, S. Crewell, T. Cronin, Z. Cui, Y. Cuypers, A. Daley, G. M. Damerell, T. Dauhut, H. Deneke, J.-P. Desbios, S. Dörner, S. Donner, V. Douet, K. Drushka, M. Dütsch, A. Ehrlich, K. Emanuel, A. Emmanouilidis, J.-C. Etienne, S. Etienne-Leblanc, G. Faure, G. Feingold, L. Ferrero, A. Fix, C. Flamant, P. J. Flatau, G. R. Foltz, L. Forster, I. Furtuna, A. Gadian, J. Galewsky, M. Gallagher, P. Gallimore, C. Gaston, C. Gentemann, N. Geyskens, A. Giez, J. Gollop, I. Gouirand, C. Gourbeyre, D. de Graaf, G. E. de Groot, R. Grosz, J. Güttler, M. Gutleben, K. Hall, G. Harris, K. C. Helfer, D. Henze, C. Herbert, B. Holanda, A. Ibanez-Landeta, J. Intrieri, S. Iyer, F. Julien, H. Kalesse, J. Kazil, A. Kellman, A. T. Kidane, U. Kirchner, M. Klingebiel, M. Körner, L. A. Kremper, J. Kretzschmar, O. Krüger, W. Kumala, A. Kurz, P. L'Hégaret, M. Labaste, T. Lachlan-Cope, A. Laing, P. Landschützer, T. Lang, D. Lange, I. Lange, C. Laplace, G. Lavik, R. Laxenaire, C. Le Bihan, M. Leandro, N. Lefevre, M. Lena, D. Lenschow, Q. Li, G. Lloyd, S. Los, N. Losi, O. Lovell, C. Luneau, P. Makuch, S. Malinowski, G. Manta, E. Marinou, N. Marsden, S. Masson, N. Maury, B. Mayer, M. Mayers-Als, C. Mazel, W. McGeary, J. C. McWilliams, M. Mech, M. Mehlmann, A. N. Meroni, T. Mieslinger, A. Minikin, P. Minnett, G. Möller, Y. Morfa Avalos, C. Muller, I. Musat, A. Napoli, A. Neuberger, C. Noisel, D. Noone, F. Nordsiek, J. L. Nowak, L. Oswald, D. J. Parker, C. Peck, R. Person, M. Philippi, A. Plueddemann, C. Pöhlker, V. Pörtge, U. Pöschl, L. Pologne, M. Posyniak, M. Prange, E. Quiñones Meléndez, J. Radtke, K. Ramage, J. Reimann, L. Renault, K. Reus, A. Reyes, J. Ribbe, M. Ringel, M. Ritschel, C. B. Rocha, N. Rochetin, J. Röttenbacher, C. Rollo, H. Royer, P. Sadoulet, L. Saffin, S. Sandiford, I. Sandu, M. Schäfer, V. Schemann, I. Schirmacher, O. Schlenczek, J. Schmidt, M. Schröder, A. Schwarzenboeck, A. Sealy, C. J. Senff, I. Serikov, S. Shohan, E. Siddle, A. Smirnov, F. Späth, B. Spooner, M. K. Stolla, W. Szkółka, S. P. de Szoeke, S. Tarot, E. Tetoni, E. Thompson, J. Thomson, L. Tomassini, J. Totems, A. A. Ubele, L. Villiger, J. von Arx, T. Wagner, A. Walther, B. Webber, M. Wendisch, S. Whitehall, A. Wiltshire, A. A. Wing, M. Wirth, J. Wiskandt, K. Wolf, L. Worbes, E. Wright, V. Wulfmeyer, S. Young, C. Zhang, D. Zhang, F. Ziemen, T. Zinner, and M. Zöger. EUREC^{4}A. *Earth System Science Data*, 13(8): 4067–4119, 2021. doi: 10.5194/essd-13-4067-2021.

K. E. Taylor, R. J. Stouffer, and G. A. Meehl. An overview of CMIP5 and the experiment design. *Bull. Am. Meteorol. Soc.*, 93:485–498, 2012. doi: 10.1175/BAMS-D-11-00094.1.